Journal of Magnetic Resonance 279 (2017) 1–10

Contents lists available at ScienceDirect

Journal of Magnetic Resonance

journal homepage: www.elsevier.com/locate/jmr

Anisotropic diffusion phantoms based on microcapillaries

Sebastian Vellmer, Daniel Edelhoff, Dieter Suter, Ivan I. Maximov *

Experimental Physics III, TU Dortmund University, Dortmund, Germany

ARTICLE INFO

Article history:
Received 26 September 2016
Revised 30 March 2017
Accepted 2 April 2017
Available online 5 April 2017

Keywords:
Diffusion MRI
Diffusion kurtosis imaging
Microcapillary
Diffusion phantom
Microimaging
Time-dependent diffusion
Axonal models

ABSTRACT

Diffusion MRI is an efficient and widely used technique for the investigation of tissue structure and organisation *in vivo*. Multiple phenomenological and biophysical diffusion models are intensively exploited for the analysis of the diffusion experiments. However, the verification of the applied diffusion models remains challenging. In order to provide a "gold standard" and to assess the accuracy of the derived parameters and the limitations of the diffusion models, anisotropic diffusion phantoms with well known architecture are demanded. In the present work we built four anisotropic diffusion phantoms consisting of hollow microcapillaries with very small inner diameters of 5, 10 and 20 μm and outer diameters of 90 and 150 μm. For testing the suitability of these phantoms, we performed diffusion measurements on all of them and evaluated the resulting data with a set of popular diffusion models, such as diffusion tensor and diffusion kurtosis imaging, a two compartment model with intra- and extra-capillary water spaces using bi-exponential fitting, and time-dependent diffusion coefficients in Mitra's limit. The perspectives and limitations of these diffusion phantoms are presented and discussed.

1. Introduction

Diffusion-weighted magnetic resonance imaging (MRI) is a very well known technique which is widely exploited in physics, biology, chemistry, and medicine. Particularly in medicine, diffusion MRI has enormous benefit and fascinating applications, for example, in the human brain studies such as the origin of pain [1], stroke diagnostics [2,3], understanding of circadian rhythms [4], neurooncology [5], and more (see Ref. [6] and references therein).

During the last decade, multiple phenomenological and biophysical diffusion models were developed in order to explain and predict the signal attenuation in different experimental setups [7–14]. However, a clear and robust interpretation of the diffusion signal decay in a macroscopic voxel in terms of the characteristic diffusion parameters remains a theoretically and computationally challenging problem [13]. In turn, artificially designed structures with well known composition and architectural organisation at micrometre scales, such as diffusion phantoms [15–23], allow one to validate diffusion models and to assess the accuracy of the derived diffusion scalar metrics [24–26]. Nevertheless, design of the diffusion phantoms is still not a trivial problem even in the case of numerically simulated phantoms [27,28].

Diffusion models of white matter are often designed by using a simplified representation consisting of sticks, cylinders, ellipsoids, spheres, etc. [29–32]. However, the implementation of complex tissue models in actual hardware is an almost impossible mission. On the other hand, the representation of an individual nerve fibre as a long, flexible, water-impermeable cylinder is a good approximation. Thus, plain fibre bundles are a frequent choice in phantom design procedures [16,19,17,69]. The plain fibres allow one to consider the diffusion in extra-axonal space only and, consequently, to simplify the mathematical description. Such types of flexible fibre bundles can be configured into typical neuronal compositions, for example, crossing, kissing, bending or branching fibres [15,33,34,25]. This type of anisotropic diffusion phantoms found extensive applications in the tests of tractographic algorithms [35,26] and in the determination of the axonal density packing [36,37].

The diffusion in intra-axonal space evokes a strong interest in both, diffusion models [38–40] as well as a source of powerful biomarkers [41]. A phantom resembling the nerve composition with intra- and extra-axonal spaces can be delineated by using capillaries with very small inner diameters [42–45]. In the present work we designed a set of phantoms based on microcapillaries with varying inner diameters from 5 up to 20 μm. Additionally, the used microcapillaries allowed us to choose different ratios between inner and outer diameter (ID/OD) from 0.22 (20/90) up to 0.033 (5/150). The range of ratios allows one to introduce an additional structural parameter which is not accessible in the case of plain fibres. However, available ID/OD values are still not

---

* Corresponding author.
E-mail address: ivan@e3.physik.tu-dortmund.de (I.I. Maximov).

http://dx.doi.org/10.1016/j.jmr.2017.04.002
1090-7807/

biologically relevant in sense of resembling the typical axonal ratio range of [0.5; 0.8].

The designed phantoms were tested by diffusion NMR microscopy in order to assess the signal attenuation from intra- and extra-capillary water. High resolution imaging allowed us to verify the applicability and validity of popular diffusion approaches such as diffusion tensor imaging (DTI) [7], diffusion kurtosis imaging (DKI) [8], bi-exponential fitting of two-compartment signal decay [14], and time-dependent diffusion coefficients [46]. As a result, we proved that the diffusion phantoms, based on microcapillaries, are robust and powerful systems for the verification of diffusion models.

2. Methods and materials

All measurements were performed using our wide-bore 14.1 T microimaging Varian system. The system is equipped with gradient coils providing amplitudes up to 3 T/m in z-direction and 2 T/m in x- and y-directions. The temperature inside of the system was monitored and equal to 15.6 °C.

2.1. Phantom construction

All phantoms were designed using the hollow flexible fused silica capillaries manufactured by Polymicro Technologies™ [47]. In order to build diffusion phantoms we used microcapillaries with IDs of 20, 10 and 5 μm and OD of 90, 150 and 150 μm, respectively. Fig. 1a shows optical microscope images of the capillary cross-sections, in Fig. 1b and c optical images of the whole samples and T_2-weighted cross sections are presented, respectively.

To fix the bundle of capillaries in place, we used glass tubes with ID of ≈1.2 mm. The glass tube was flame-sealed on one side and a bundle of the microcapillaries was inserted. In order to assure that water fills the whole sample, without air remaining in the intra- and extra-capillary spaces, we put the NMR tube into distiled water at a reduced pressure of 100 mbar for a few hours. In order to test the water filling of phantoms we performed a visual inspection of a few slices in each phantom using *Protocol I* without diffusion weightings (see Table 2). The results of testing images for the phantom I are presented in Fig. 2. The partially darkened slices are caused by the problems with volume shimming and used coil sensitivity.

Afterwards, the water-filled NMR tube was sealed off with silicone. Diffusion measurements often suffer from vibrations generated by the rapidly switching diffusion gradients. In order to prevent motion artefacts, we increased the outer diameter to 5 mm using adhesive tape so that the whole phantom fits the 5 mm probehead (see Fig. 1b). Table 1 summarises the structural parameters of all phantoms. The values presented in Table 1 are explained in Fig. 3a, which exhibits three important features of the designed diffusion phantoms: variations in diameters and densities of the used microcapillaries; the known volume fraction of the intra- and extra-capillary water; and the surface-to-volume fraction.

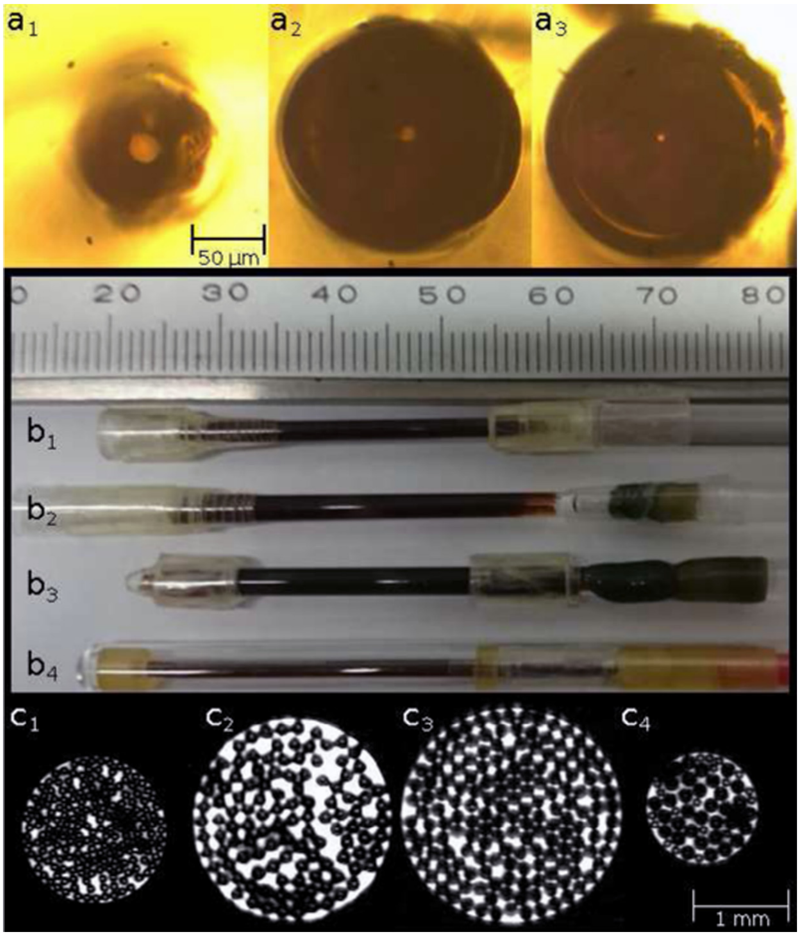

Fig. 1. Four designed diffusion phantoms. (a) Optical microscope images of the individual microcapillaries: (a_1) ID 20 μm, OD 90 μm; (a_2) ID 10 μm, OD 150 μm; (a_3) ID 5 μm, OD 150 μm. (b) Photographs of the designed phantoms: (b_1) is phantom I; (b_2) is phantom II; (b_3) is phantom III; (b)$_4$ is phantom IV; (c) T_2-weighted axial images of the water-filled phantoms I–IV.

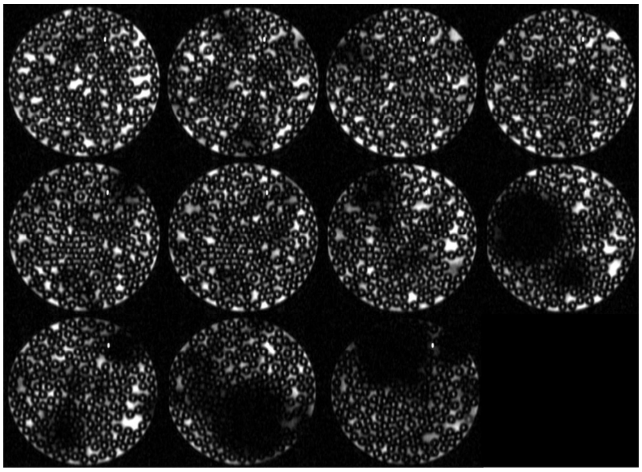

Fig. 2. Multi-slice T_2-weighted image of phantom I. A set of slices allowed us to inspect a goodness of phantom water filling and microcapillary alignment. The slice thickness is 1 mm, the in-plane resolution is $4 \times 4\ \mu\text{m}^2$.

2.2. Experimental protocols

We measured water diffusion using three pulse sequences: the classical Stejskal-Tanner (ST) sequence [48] with and without an imaging block, and a recently developed isotropically weighted diffusion sequence: FAst MEan Diffusion (FAMED) [49,50]. The z-axis of our coordinate system lies along the capillary axis. The used sequence schemes are presented in Fig. 4.

The isotropic diffusion weighting scheme employs a designed orthogonality of the $q(t)$-vector entries along the time axis, i.e. $\int_0^{TE} q_i(t)q_j(t)dt = \delta_{ij}$, where TE is the echo time and $\delta_{ii} = 1$ is the Kronecker function, and $q(t) = \gamma \int_0^t G(\tau)d\tau$. In the case of Gaussian diffusion, one can weigh the elements of second order symmetric diffusion tensor in such a manner that all off-diagonal terms would be suppressed [49–52]. To satisfy the orthogonality condition for $q(t)$-entries we use simple (co)sine modulations (see a notation in Fig. 4):

$$\vec{G}(t) = G\begin{cases} \begin{pmatrix} \frac{1}{2}\cos\left(\frac{2\pi}{\Delta}t\right) \\ \frac{1}{\sqrt{3}}\sin\left(\frac{4\pi}{\Delta}t\right) \\ \cos\left(\frac{4\pi}{\Delta}t\right) \end{pmatrix}, & \text{if } 0 < t \leqslant \frac{\Delta}{2}. \\ \vec{0}, & \text{if } \frac{\Delta}{2} < t \leqslant \frac{\Delta}{2} + t_{180}. \\ -\begin{pmatrix} \frac{1}{2}\cos\left(\frac{2\pi}{\Delta}(t - t_{180})\right) \\ \frac{1}{\sqrt{3}}\sin\left(\frac{4\pi}{\Delta}(t - t_{180})\right) \\ \cos\left(\frac{4\pi}{\Delta}(t - t_{180})\right) \end{pmatrix}, & \begin{pmatrix} \text{if } \frac{\Delta}{2} + t_{180} < t. \\ t \leqslant \Delta + t_{180}. \end{pmatrix} \end{cases} \quad (1)$$

The corresponding b-value of FAMED is

$$b_{\text{FAMED}} = \sum_i \int_0^{TE} q_i(t)q_i(t)dt = G^2\gamma^2 \frac{3\Delta^3}{32\pi^2}. \quad (2)$$

As a result, the signal decay can be estimated as a simple exponential decay $S = S_0 \exp(-b \cdot \text{MD})$, where S_0 is the signal without diffusion weighting, and MD is the mean diffusion.

The three sequences are represented by their protocols:

Protocol I: ST sequence with imaging block. We used conventional DTI protocol with three mutually orthogonal diffusion directions. The voxel size is $4 \times 4 \times 10^3\ \mu\text{m}^3$.

Protocol II: ST sequence without imaging block with diffusion weighting gradients directed in both directions, parallel as well as perpendicular to the microcapillary orientation.

Protocol III: It repeats protocol II with the FAMED sequence [49,50].

The sequences parameters for all protocols are summarised in Table 2.

2.3. Numerical simulations

The designed diffusion phantoms grant a unique opportunity to establish a comparison of the performed measurements with numerical simulations using the well known phantom structure. In the case of simple geometries such as infinite cylinders one can estimate the signal attenuation using a method of multiple correlation functions (MCF) [9,10]. In our work we used Matlab MCF library written by Denis Grebenkov. The MCF approach allowed us to compute the theoretical signal decay for intra-capillary water diffusion for IDs of 10 and 20 µm and predict an apparent diffusion coefficient D_{xx}^{sim}.

The complex diffusion of water molecules in the phantoms might be modelled by Monte Carlo (MC) simulations. In order to reproduce the geometrical constraints of the phantoms we used binary masks rendered from T_2-weighted images (see Fig. 3b). We converted the binary masks to a Cartesian grid in the x-y-plane with a constant step $\Delta r = 0.1\ \mu\text{m}$.

In the case of the Monte Carlo simulations we used number of particles N equals to 10^7. The trajectory of an individual particle is generated by a random walk process. In each time step $\delta t = \Delta r^2/4D_0$ a particle performs one step to a randomly chosen neighbour place on the grid, where $D_0 = 1.8 \cdot 10^{-3}\ \text{mm}^2/\text{s}$ is the diffusion coefficient of free water, and $\delta t = 1.4\ \mu\text{s}$ is the used time step. The z-component of each particle trajectory, which is only important for the FAMED sequence, is supposed to be the Gaussian. Time-dependent gradients are discretised in accordance with the time step δt. As a result, at the end of the spin-echo experiment the particles accumulated a phase change $\phi_i = \gamma \sum_j G(t_j)r_i(t_j)\delta t$, and the synthetic signal attenuation can be estimated by a summing over all particles: $S = \sum_j \exp(i\phi_j)$ [53]. At the beginning, we compared MCF solutions for cylinders with IDs 10 and 20 µm in order to verify an accuracy of the chosen MC parameters.

All curves were fitted using Matlab. In the case of linearised mono-exponential fitting we used *fit*-function, the logarithmised kurtosis signal was fitted using *fit*-function and linear least squares method. In order to estimate the parameters of the bi-exponential model we used *lsqcurvefit*-function with applied constraints: volume fraction $f \subset [0; 0.5]$, extra-capillary diffusion coefficient

Table 1
The parameters of the designed diffusion phantoms. Phantom numeration is the same as in Fig. 1. The parameter meaning is explained in Fig. 3.

Phantom model	Number of capillaries			Phantom diameter (mm)	Intra-capillary water fraction $\rho = V_{ic}/(V_{ec} + V_{ic})$	Surface-to-volume ratio $(\text{m}^{-1}) \cdot 10^4$
	20 µm	10 µm	5 µm			
I	190	0	0	1.50	0.11	6.6
II	0	95	0	2.07	$4.4 \cdot 10^{-3}$	3.2
III	0	0	156	2.25	$7.7 \cdot 10^{-6}$	6.8
IV	19	20	13	1.17	$2.1 \cdot 10^{-2}$	7.1

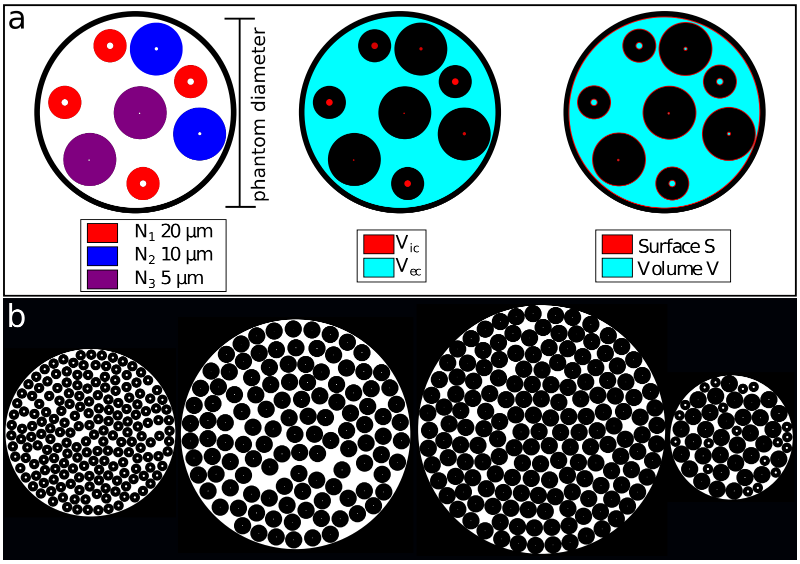

Fig. 3. (a) Schematic representation of main phantom parameters. N_i is the number of used capillaries with ID $k = 20, 10, 5$ µm (left). V_{ic} is intra- and V_{ec} is extra-capillary water volumes (centre), and the surface-to-volume geometry (right). (b) Masks for the Monte Carlo simulation. The masks are rendering phantom structures in Fig. 1c. A pixel size corresponds to 1×1 µm^2.

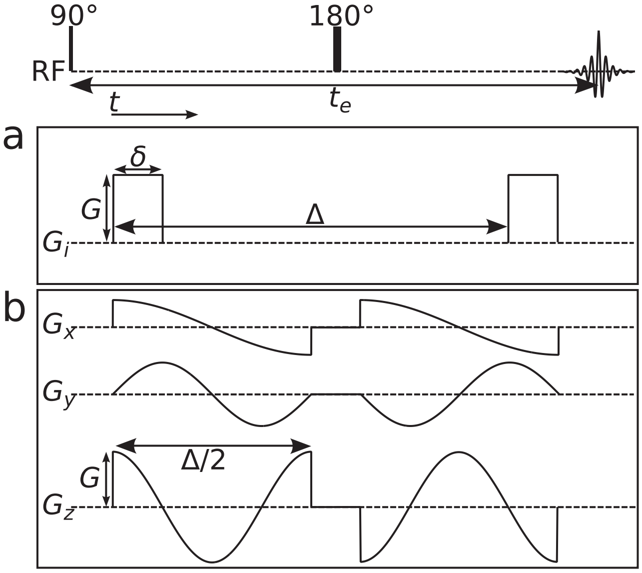

Fig. 4. Schematic representation of the used diffusion pulse sequences. (a) Conventional Stejskal-Tanner sequence; (b) isotropically weighted FAMED sequence [49].

$D_{ec} \subset [0; 2] \cdot 10^{-3}$ mm^2/s, and intra-capillary diffusion coefficient $D_{ic} \subset [0; 1.5] \cdot 10^{-3}$ mm^2/s. We used the *trust-region-reflectivity* algorithm. The constrained optimisation procedure strongly depends on the used initial guess. In our model the initial guesses were $D_{ec} = 1.7 \cdot 10^{-3}$ mm^2/s, $D_{ic} = 0.5 \cdot 10^{-3}$ mm^2/s and $f = 0.1$.

3. Results

3.1. Diffusion tensor imaging

In order to detect and visualise the intra- and extra-capillary diffusion, we chose the phantom IV and protocol I. The resulting images are presented in Fig. 5. The blurring effect in Fig. 5 might originate from both, the motion artefacts (vibrations) produced by fast switching gradients, as well as the very small voxel size, with a characteristic diffusion length $l \approx 19$ µm which is higher then the voxel size 4 µm. The capillary walls (OD = 90 and 150 µm) are invisible in NMR. The signal from capillaries with ID = 5 µm is almost invisible due to a very low signal-to-noise ratio (SNR). Voxels localised on the outer face of the microcapillaries are also distorted by susceptibility artefacts due to the high magnetic field gradient as well as by the partial volume effect due to the large slice thickness of 1 mm. Using the known capillary axes orientation and invoking axial symmetry, we can determine the typical diffusion parameters such as mean diffusivity (MD) and fractional anisotropy (FA) by a linear fitting of the logarithmised signal decay. The scalar DTI diffusion metrics are presented in Fig. 5d and e, respectively.

The high spatial resolution of the images allowed us to distinguish the signals from intra- and extra-capillary regions and separately determine averaged values of the diffusion DTI scalar metrics such as D_{xx}, D_{yy}, D_{zz}, MD and FA. Spatial averages were performed using the manually selected regions of interest (ROI), namely: extra-capillary space, intra-capillary spaces: for ID = 20 and 10 µm (for the ROI see Appendix Fig. 9). The averaged DTI diffusion values are summarised in Table 3. The histograms of MD and FA scalar metrics demonstrate two separate peaks associated

Table 2
Sequence parameters of the used protocols. Diffusion time Δ, duration of rectangular pulse δ, echo time (TE), repetition time (TR), number of excitations (NEX). Range of values is presented as [min:step:max].

Protocol	Δ (ms)	δ (ms)	*b*-value (s/mm^2)	TE (ms)	TR (s)	NEX
I	40	1	0,1000	50	10	20
II	[40:10:100]	1	[0:300:3000]	[50:10:110]	10	8
III	[40:10:100]	–	[0:300:3000]	[50:10:110]	10	8

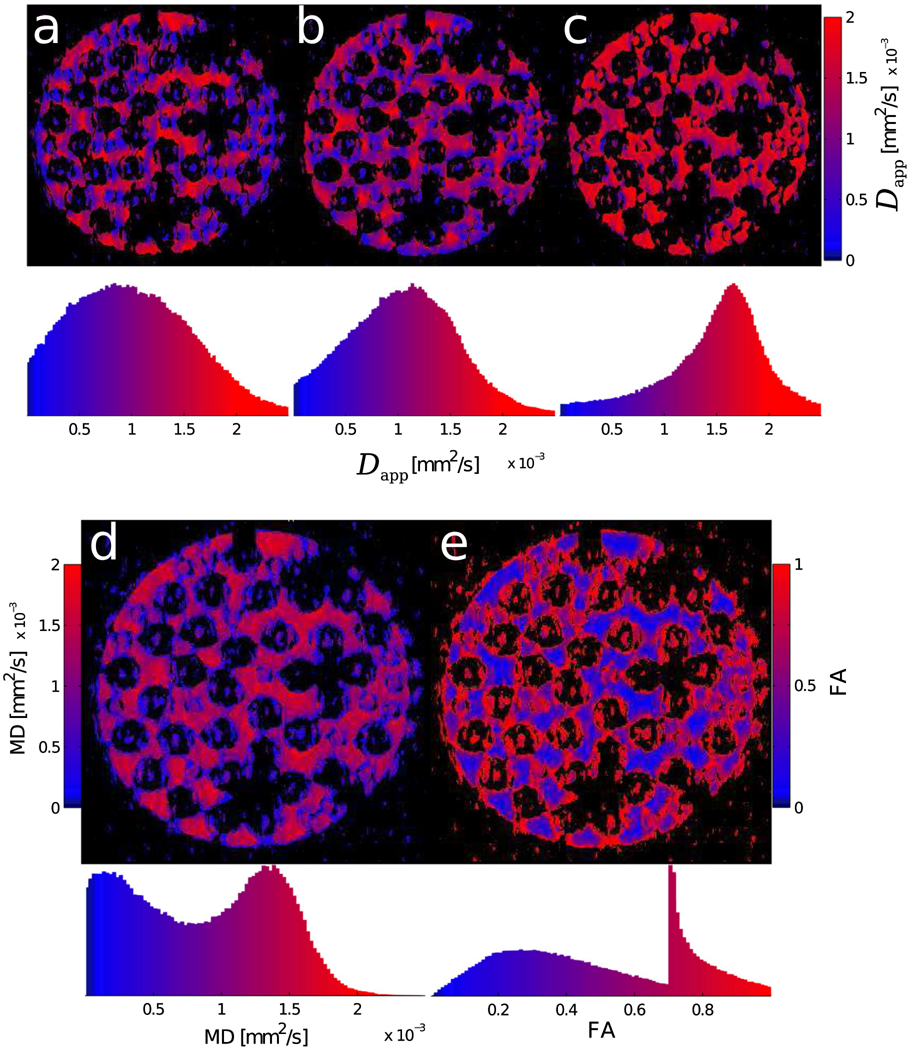

Fig. 5. High resolution images of the phantom IV. (a)–(c): Measured apparent diffusion coefficients $D_{\rm app}$ for phantom IV along the mutually orthogonal directions x, y, and z, respectively. The main axis of the capillaries lies along the z direction. Diffusion scalar metrics are presented by: mean diffusivity (d) and fractional anisotropy (e). The histograms present a distribution of scalar metrics in accordance to the same colour scheme as well as in the image.

Table 3
Spatially averaged DTI scalar metrics such as the apparent diffusion coefficients $D_{\rm app}$, MD and FA for three ROIs of phantom IV (see Fig. 5). The used ROIs are presented in Appendix Fig. 9.

Values	Extra-capillary space	intra-capillary space	
		20 µm	10 µm
D_{xx} (mm²/s) · 10^{-3}	1.6 ± 0.3	0.6 ± 0.5	0.4 ± 0.3
D_{yy} (mm²/s) · 10^{-3}	1.5 ± 0.2	0.9 ± 0.5	0.5 ± 0.4
D_{zz} (mm²/s) · 10^{-3}	1.6 ± 0.2	1.7 ± 0.6	1.8 ± 0.7
MD (mm²/s) · 10^{-3}	1.6 ± 0.1	1.0 ± 0.3	0.9 ± 0.3
FA	0.15 ± 0.07	0.6 ± 0.2	0.7 ± 0.2

with intra- and extra-capillary pools of the phantom. Notably, that the FA histogram exhibits the strong peak for intra-capillary values.

At the same time the signal from single microcapillary can be estimated using analytic approach. The D^{sim}_{xx} values determined with the MCF approach by Grebenkov [9,10] fit the experimental results: ID 20 µm: $D^{sim}_{xx} = 0.55 \cdot 10^{-3}$ mm²/s; ID 10 µm: $D^{sim}_{xx} = 0.14 \cdot 10^{-3}$ mm²/s (see Supplementary Materials for the details). The strong variation of the experimental results is stipulated by the mentioned above imaging artefacts.

3.2. Apparent diffusion: mono-exponential decay

In this test we measured all phantoms using the protocols II and III. In order to estimate the mono-exponential signal decay, we considered only b-values lower than 10^3 mm²/s. The diffusion signal decay in the case of the Gaussian diffusion is

$$\ln\left(\frac{S(b)}{S_0}\right) = -bD_{app}, \qquad (3)$$

where D_{app} is the apparent diffusion coefficient, S_0 is the signal without diffusion weighting. $D_{\rm app}$ for each phantom was estimated by linear fitting. The results are presented in Fig. 6. In the case of the FAMED sequence the calculated diffusion coefficient represents the MD [49,50]. The solid lines in Fig. 6 represent the time dependence obtained from the MC simulations.

The values for free water are the references. The literature value is $1.81 \cdot 10^{-3}$ mm²/s [54] for a temperature of 15.6 °C.

3.3. Apparent diffusion: kurtosis expansion

In order to detect a deviation of the water diffusion from the Gaussian behaviour, we used data with all b-values from the protocols II and III from measurements with all four phantoms and

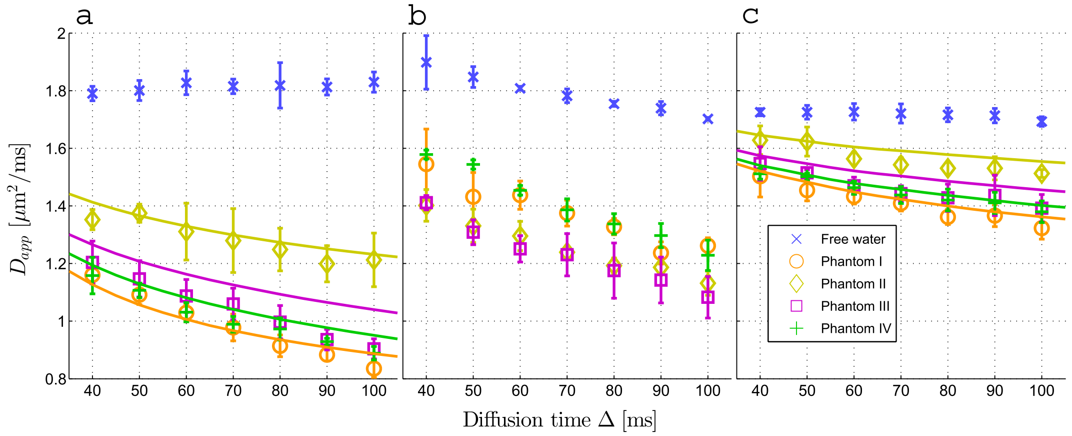

Fig. 6. Apparent diffusion coefficients D_{app} in the case of mono-exponential signal decay. (a) D_{app} obtained by ST sequence perpendicular to the main phantom axis; (b) D_{app} obtained by ST sequence along to the main phantom axis; and (c) MD values obtained by FAMED sequence. Solid lines are the results of the MC simulations.

free water. The non-Gaussianity metrics were determined by using second order expansion of the diffusion signal [8]. The diffusion signal in this case can be represented as

$$\ln\left(\frac{S(b)}{S_0}\right) = -bD_{app} + \frac{1}{6}(bD_{app})^2 K_{app}, \tag{4}$$

where D_{app} and K_{app} are the apparent diffusion and kurtosis coefficients, respectively. The estimated apparent diffusion and kurtosis coefficients resulting from fitting of the data using *b*-values up to 3000 s/mm^2 are presented in Fig. 7. The solid lines in Fig. 7 represent the time dependence obtained from the MC simulations.

3.4. Apparent diffusion: bi-exponential signal fitting

The diffusion model consisting of two independent compartments such as intra- and extra-capillary spaces can be described as a bi-exponential signal decay:

$$\frac{S(b)}{S_0} = f \cdot \exp(-bD_{ic}) + (1-f) \cdot \exp(-bD_{ec}), \tag{5}$$

where *f* is the volume fraction between two signal components contributing to the final decay with intra-capillary diffusion D_{ic} and extra-capillary diffusion D_{ec} coefficients. The results of the bi-exponential assessments are presented in Fig. 8. To demonstrate the goodness of fit the coefficient of determination R^2 [55] is used. The solid lines in Fig. 8 represent the time dependence obtained from the MC simulations.

3.5. Time-dependent diffusion coefficients

In the short diffusion time limit, the time dependence of the diffusion coefficient is described by the expression

$$D(t) = D_0\left(1 - \frac{4}{3d\sqrt{\pi}}\frac{A}{V}\sqrt{D_0 t}\right), \tag{6}$$

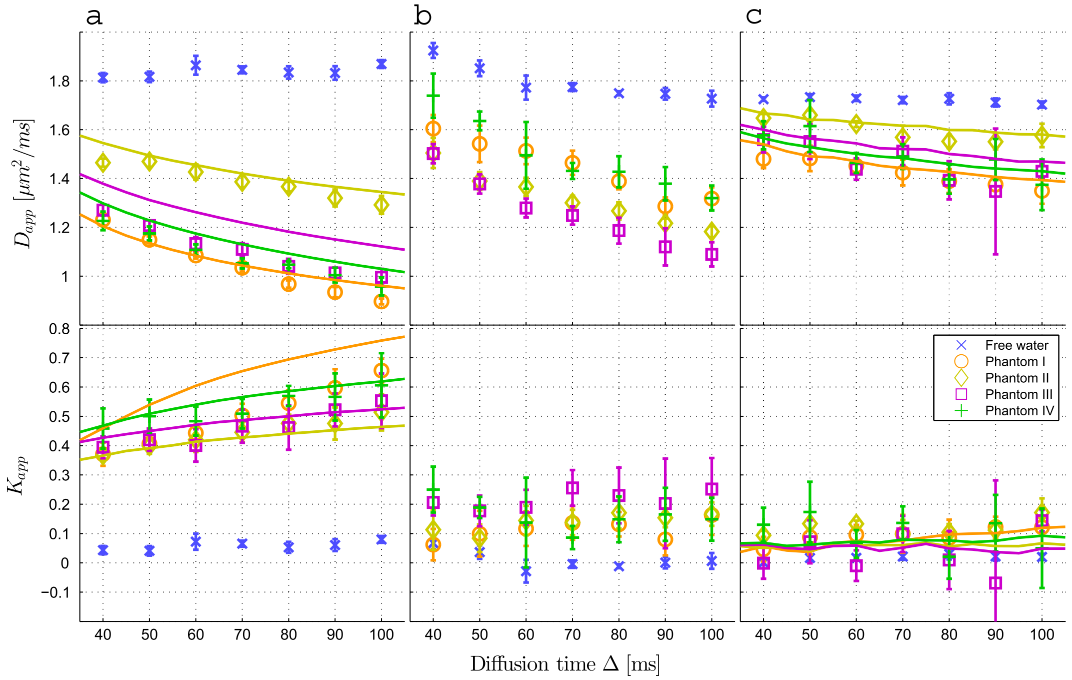

Fig. 7. Apparent diffusion D_{app} and kurtosis K_{app} coefficients for four diffusion phantoms and free water. The data were measured using the ST sequence in *x* (a) and *z* (b) directions. The data obtained with the FAMED sequence are presented in panel (c). The error bars represent the 95% confident intervals. Solid lines are the results of the MC simulations.

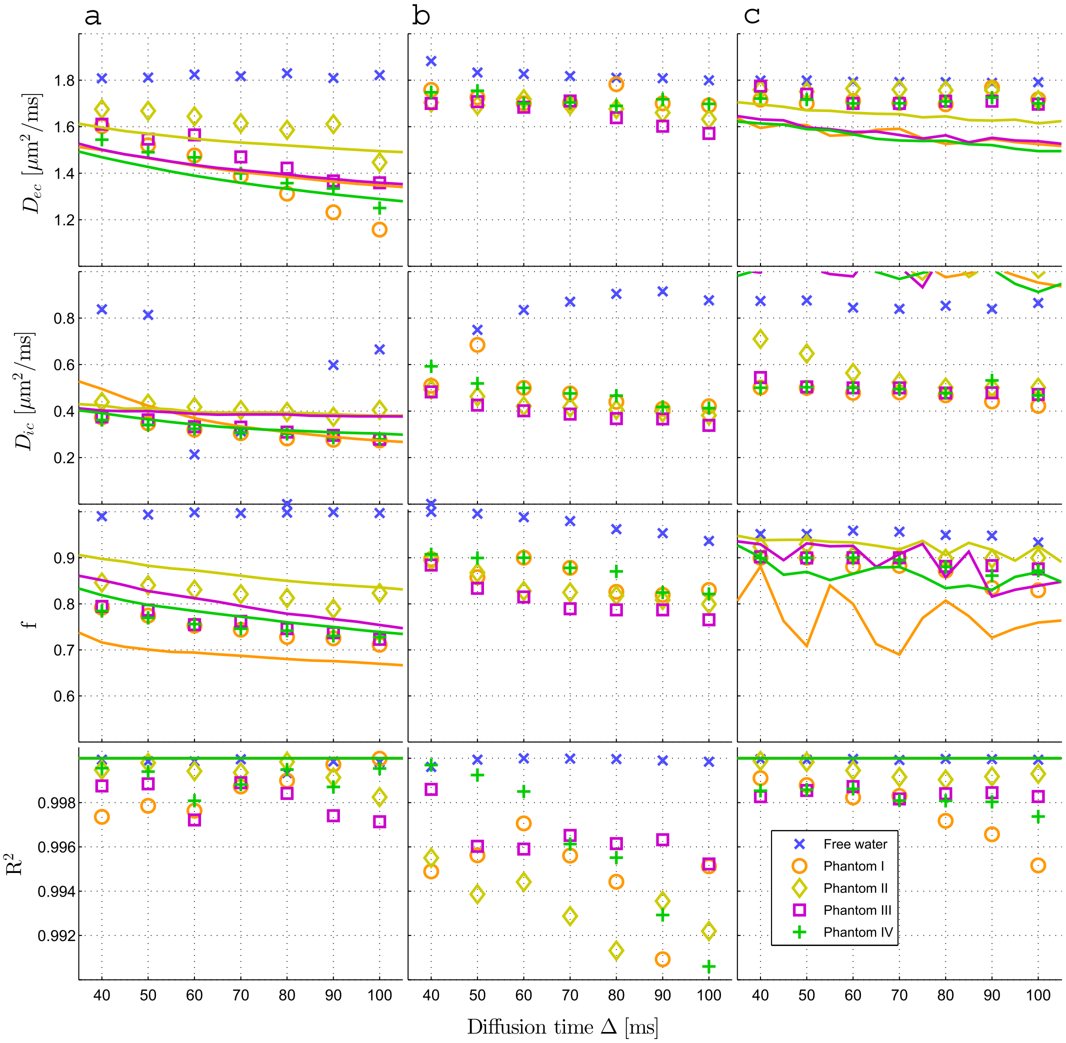

Fig. 8. Apparent diffusion coefficients and volume fractions *f* of intra- (D_{ic}) and extra-capillary (D_{ec}) water for four diffusion phantoms and free water are presented. The data were measured with the ST sequence in perpendicular *x* (a) and longitudinal *z* (b) directions. The FAMED results for bi-exponential fitting are presented in panel (c). Solid lines are the results of the MC simulations.

of Mitra et al. [56], with the diffusion constant of free water $D_0 = 1.81 \cdot 10^{-3}$ mm^2/s [54], the surface-to-volume ratio (SVR) A/V and the characteristic dimension *d*. The time-dependent apparent diffusion coefficients estimated from the mono-exponential and the kurtosis expansion models were used in order to determine the SVR values. The results are presented in Table 4.

4. Discussion

A validation of phenomenological and biophysical diffusion models using ground truth information is a very important and challenging problem of diffusion MRI. In order to overcome the typical obstacles related to frequently used phantoms with plain fibres, gels, and others, we designed and tested four anisotropic diffusion phantoms based on microcapillaries with IDs of 5, 10, and 20 µm. The phantoms allowed us to validate various techniques for diffusion measurement often used in clinical settings, namely, mono-exponential, cumulant expansion, bi-exponential fittings, and time-dependence of the diffusion coefficients in Mitra's limit. We demonstrated that the phantoms consisting of microcapillaries are useful and provide advanced modelling features such as intra- and extra-capillary spaces, high anisotropy,

Table 4
Surface-to-volume ratio (SVR) using Mitra's limit [56] for four phantoms. We used two sets of time-dependent diffusion coefficients obtained from the mono-exponential and kurtosis expansion approaches. The original phantom parameters are presented in Table 1.

Sequence	Fitting	SVR $(\mathrm{m}^{-1}) \cdot 10^4$ of Phantom			
		I	II	III	IV
–	Geometrical	6.6	3.2	6.8	7.1
ST	Kurtosis based	5.1 ± 0.1	2.8 ± 0.1	4.6 ± 0.1	4.8 ± 0.2
	Mono-exponential based	5.4 ± 0.1	3.5 ± 0.2	5.0 ± 0.1	5.2 ± 0.2
FAMED	Kurtosis based	7.7 ± 0.3	4.2 ± 0.4	6.9 ± 0.9	6.5 ± 0.9
	Mono-exponential based	8.0 ± 0.2	4.9 ± 0.3	6.9 ± 0.2	7.2 ± 0.2

set of g-factors, known surface-to-volume ratio and water volume fractions, and radii distribution.

One of the main questions in diffusion MRI is, if is it possible to determine an intra-axonal diameter within the clinically achievable hardware setups. There are many theoretical and experimental attempts to assess the intra-axonal diameter using diffusion phantoms [57–59] as well as *in vivo* experiments [40,38]. The present work shows that even in the case of high-resolution microimaging NMR, the signal from capillaries lower than 5 μm is problematic (see Fig. 5). However, the capillaries with ID of 10 and 20 μm exhibited promising results, in particular, in the case of the diffusion scalar metrics. The averaged metrics such as the apparent diffusion coefficients, MD and FA are in a good agreement with the expected values (see Table 3). Problems related to the small voxel size of the microimaging should be taken into account, such as additional distortions from motion artefacts and susceptibility distortions, one expects to have an influence of the surface relaxation for the fused silica capillaries, in particular, inside of the cavities [60]. The surface relaxation effect might explain the high FA metrics posed close to the external microcapillary walls (see Fig. 5).

The apparent diffusion coefficients and MD values determined from mono-exponential and second-order expansion of diffusion signal are typical scalar metrics used as characteristic tissue parameters [70]. It is particularly interesting to investigate the changes of diffusion metrics estimated by mono-exponential and second-order expansion fittings depending on the diffusion times [61]. The results obtained by mono-exponential fitting approach are underestimated diffusion coefficients compared to the kurtosis based approach (see Figs. 6 and 7) at the longer diffusion times. The effect diffusion metric discrepancy was already revealed earlier in brain studies [62]. In the case of Gaussian diffusion, such as along main phantom axis or isotropic weighted sequences, kurtosis based metrics have a smaller deviation for all diffusion times. For diffusion perpendicular to the main phantom axis, we found significantly increased kurtosis metrics with increasing diffusion times (see Fig. 7). Some difference between the MC simulations and experimental data for the long diffusion times might originate from above mentioned artefacts and relaxation effects. Notably, the FAMED-based scalar metrics exhibit a good agreement with the MC simulations comparing to the conventional ST sequence.

Attempts to determine the signal contributions from different diffusion compartments have been made many times [63,39]. However, a reliable signal decomposition was almost impossible to evaluate robustly due to fine effects and complexity of the used subjects and an absence of a “gold standard”. Application of our phantoms allowed us to perform an exact comparison between the signal fits and real compartments since the geometry of the phantoms are determined with high accuracy. As one can see in Fig. 8, if the intra- and extra-capillary diffusion coefficients exhibit adequate values, the volume fraction f has significant bias. We assume that the bias of water volume fraction can be stipulated by the constrained optimisation algorithm which is very sensitive to a noise presence and selection of initial guesses. Only in the case of phantom I where the intra-capillary fraction is very high the f-fraction estimation is close to the true value (see Fig. 8b). Moreover, in the case of longitudinal and isotropic weighted scheme the diffusion coefficients for both intra- and extra-capillary spaces demonstrated very weak time dependence (see Fig. 8b and c). In Fig. 8a we found a strong time-dependence of the diffusion coefficients for the extra-capillary water. Interestingly, the isotropic weighted sequence FAMED provided results almost independent of the phantom structures in contrast to the conventional ST sequence, in particular, for the perpendicular diffusion direction. The free water sample also caused problems for the fitting due to zero ratio of intra-capillary water and complications related to the constrained optimisation.

The time-dependence of the diffusion coefficients is a very attractive approach for determining the diffusion parameters and axonal structure parameters. Two diffusion time limits are currently used for diffusion MRI [46]: a short diffusion time limit [56] (also known as Mitra’s limit) and a tortuosity limit [13]. Experimentally, these two regimes are exploited in oscillating diffusion gradients [12] in order to achieve the shortest diffusion times and with stimulated echoes [13] in order to suppress relaxation artefacts. We tried to provide the estimations using our phantoms in the case of short diffusion time limits using the conventional ST sequence and isotropic weighted scheme. The shortest diffusion time was equal to 40 ms, which can be considered as close to the short time limit of Mitra. In this case the diffusion length of free water is $l_D = 12$ μm, which is within the range of the inner diameters used in our phantoms. However, for the diffusion times of $\approx$ 100 μs, this is no longer fulfilled. Nevertheless, the obtained results demonstrated excellent agreement with geometrical estimations for the phantoms (see Table 4).

As a possible limitation we have to mention that the g-ratio between inner and outer diameters for the capillaries of 5 (and accessible but not used at the moment 2) μm is very far away from the real g-factor in the human brain axons. At the same time an arbitrary composition of the microcapillary phantoms might lead to the irregular shapes of the extra-capillary space, i.e. to the possibly strong internal magnetic gradients even in the case of parallel main magnetic field to the capillary axes. Besides the possible internal field distortions, an order of the surface relaxation effect for the fused silica microcapillaries should be estimated as well. Another limitation is an absence of water permeability of the capillary walls, which excludes the possibility of using it for modelling myelin water. However, we expect that progress in material science will overcome this point soon [64,65].

5. Conclusion

The designed anisotropic diffusion phantoms based on the flexible fused silica microcapillaries with inner diameters in the range of a few microns allowed us to construct complex diffusion models and to perform an accurate validation of different phenomenological diffusion models. In the future we plan to build phantoms

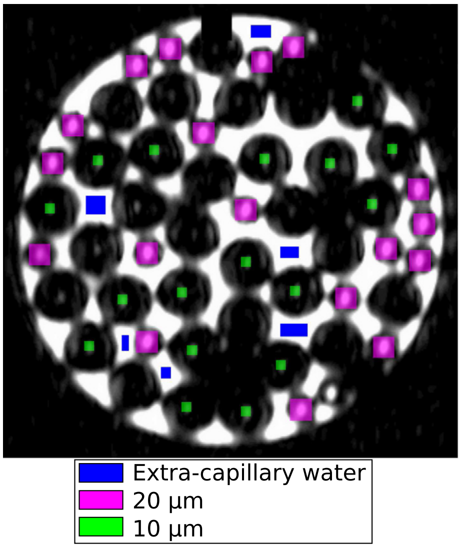

Fig. 9. Manually chosen regions of extra- and intra-capillary water with ID = 20 and 10 μm.

mimicking anatomical structures such as corpus callosum or precortical white matter regions with a good histological credibility. As a result, the designed phantoms are good candidates for a calibration of the experimental setups using hyperpolarised substances [66,67] or diffusion gradient shape optimisation [59,68].

Acknowledgements

The work was financially supported by the DFG Grant SU 192/32-1. IIM gratefully thanks PD Dr. Valerij G. Kiselev for fruitful discussions.

Appendix A

For masking the typical regions with extra-capillary, and intra-capillary regions we used high resolution T_2-weighted image. The regions were drawn manually in each case. The resulting mask is presented in Fig. 9.

Appendix B. Supplementary material

Supplementary data associated with this article can be found, in the online version, at http://dx.doi.org/10.1016/j.jmr.2017.04.002.

References

[1] T. Warbrick, V. Fegers-Stollenwerk, I.I. Maximov, F. Grinberg, N.J. Shah, Using structural and functional brain imaging to investigate responses to acute thermal pain, J. Pain 17 (2016) 836–844.

[2] C.H. Sotak, The role of diffusion tensor imaging in the evaluation of ischemic brain injury - a review, NMR Biomed. 15 (2002) 561–569.

[3] R.A. Weber, E.S. Hui, J.H. Jensen, X. Nie, M.F. Falangola, J.A. Helpern, D.L. Adkins, Diffusional kurtosis and diffusion tensor imaging reveal different time-sensitive stroke-induced microstructural changes, Stroke 46 (2015) 545–550.

[4] J. Rosenberg, I.I. Maximov, M. Reske, F. Grinberg, N.J. Shah, Early to bed, Early to rise: diffusion tensor imaging identifies chronotype-specificity, Neuroimage 84 (2014) 428–434.

[5] B.M. Ellingson, M. Bendszus, A. Sorensen, W.B. Pope, Emerging techniques and technologies in brain tumor imaging, Neuro-Oncol. 16 (2014) vii12–vii23.

[6] H. Jonhansen-Berg, T. Behrens, Diffusion MRI: From Quantitative Measurement to In Vivo Neuroanatomy, Elsevier, 2013.

[7] P.J. Basser, J. Mattiello, D. LeBihan, MR diffusion tensor spectroscopy and imaging, Biophys. J. 66 (1994) 259.

[8] J.H. Jensen, J.A. Helpern, A. Ramani, H. Lu, K. Kaczynski, Diffusional kurtosis imaging: the quantification of non-gaussian water diffusion by means of magnetic resonance imaging, Magnet. Reson. Med. 53 (2005) 1432–1440.

[9] D.S. Grebenkov, Laplacian eigenfunctions in NMR. I. A numerical tool, Conc. Magnet. Reson. Part A 32 (2008) 277–301.

[10] D.S. Grebenkov, Laplacian eigenfunctions in NMR. II. Theoretical advances, Conc. Magnet. Reson. Part A 34 (2009) 264–296.

[11] C. Liu, R. Bammer, B. Acar, M.E. Moseley, Characterizing non-gaussian diffusion by using generalized diffusion tensors, Magnet. Reson. Med. 51 (2004) 924–937.

[12] M. Schachter, M.D. Does, A.W. Anderson, J.C. Gore, Measurements of restricted diffusion using an oscillating gradient spin-echo sequence, J. Magnet. Reson. 147 (2000) 232–237.

[13] D.S. Novikov, J.H. Jensen, J.A. Helpern, E. Fieremans, Revealing mesoscopic structural universality with diffusion, Proc. Natl. Acad. Sci. USA 111 (2014) 5088–5093.

[14] V.G. Kiselev, K.A. Il'yasov, Is the biexponential diffusion biexponential?, Magnet Reson. Med. 57 (2007) 464–469.

[15] M. Perrin, C. Poupon, B. Rieul, P. Leroux, A. Constantinesco, J.-F. Mangin, D. LeBihan, Validation of q-ball imaging with a diffusion fibre-crossing phantom on a clinical scanner, Philos. Trans. R. Soc. Lond. B: Biol. Sci. 360 (2005) 881–891.

[16] E. Fieremans, Y. De Deene, S. Delputte, M.S. Ozdemir, E. Achten, I. Lemahieu, The design of anisotropic diffusion phantoms for the validation of diffusion weighted magnetic resonance imaging, Phys. Med. Biol. 53 (2008) 5405–5419.

[17] E. Fieremans, Y. De Deene, S. Delputte, M.S. Ozdemir, Y. D'Asseler, J. Vlassenbroeck, K. Deblaere, E. Achten, I. Lemahieu, Simulation and experimental verification of the diffusion in an anisotropic fiber phantom, J. Magnet. Reson. 190 (2008) 189–199.

[18] T. Zhu, R. Hu, X. Qiu, M. Taylor, Y. Tso, C. Yiannoutsos, B. Navia, S. Mori, S. Ekholm, G. Schifitto, Quantification of accuracy and precision of multi-center DTI measurements: a diffusion phantom and human brain study, Neuroimage 56 (2011) 1398–1411.

[19] R. Lorenz, B.W. Kreher, J. Hennig, M.E. Bellemann, K.A. Il'yasov, Anisotropic fiber phantom for DTI validation on a clinical scanner, Proc. Int. Soc. Magnet. Reson. Med. (2006) 2738.

[20] L. Avram, Y. Assaf, Y. Cohen, The effect of rotational angle and experimental parameters on the diffraction patterns and micro-structural information obtained from q-space diffusion NMR: implication for diffusion in white matter fibers, J. Magnet. Reson. 169 (2004) 30–38.

[21] D. Benjamini, U. Nevo, Estimation of pore size distribution using concentric double pulsed-field gradient NMR, J. Magnet. Reson. 230 (2013) 198–204.

[22] H. Li, J.C. Gore, J. Xu, Fast and robust measurement of microstructural dimensions using temporal diffusion spectroscopy, J. Magnet. Reson. 242 (2014) 4–9.

[23] N. Shemesh, E. Özarslan, P.J. Basser, Y. Cohen, Measuring small compartmental dimensions with low-q angular double-PGSE NMR: the effect of experimental parameters on signal decay, J. Magnet. Reson. 198 (2009) 15–23.

[24] I. Lavdas, K.C. Behan, A. Papadaki, D.W. McRobbie, E.O. Aboagye, A phantom for diffusion-weighted MRI (DW-MRI), J. Magnet. Reson. Imaging 38 (2013) 173–179.

[25] C. Reischauer, P. Staempfli, T. Jaermann, P. Boesiger, Construction of a temperature-controlled diffusion phantom for quality control of diffusion measurements, J. Magnet. Reson. Imaging 29 (2009) 692–698.

[26] P. Fillard, M. Descoteaux, A. Goh, S. Gouttard, B. Jeurissen, J. Malcolm, A. Ramirez-Manzanares, M. Reisert, K. Sakaie, F. Tensaouti, Quantitative evaluation of 10 tractography algorithms on a realistic diffusion mr phantom, Neuroimage 56 (2011) 220–234.

[27] A. Szafer, J. Zhong, A. Anderson, J.C. Gore, Diffusion-weighted imaging in tissues: theoretical models, NMR Biomed. 8 (1995) 289–296.

[28] C. Yeh, B. Schmitt, D. Le Bihan, J. Li-Schlittgen, C. Lin, C. Poupon, Diffusion microscopist simulator: a general monte carlo simulation system for diffusion magnetic resonance imaging, Plos One 8 (2013) e76626.

[29] G.J. Stanisz, A. Szafer, G.A. Wright, R.M. Henkelman, An analytical model of restricted diffusion in bovine optic nerve, Magnet. Reson. Med. 37 (1997) 103–111.

[30] T.E.J. Behrens, M.W. Woolrich, M. Jenkinson, H. Johansen-Berg, R.G. Nunes, S. Clare, P.M. Matthews, J.M. Brady, S.M. Smith, Characterization and propagation of uncertainty in diffusion-weighted MR imaging, Magnet. Reson. Med. 50 (2003) 1077–1088.

[31] D.C. Alexander, P.L. Hubbard, M.G. Hall, E.A. Moore, M. Ptito, G.J.M. Parker, T.B. Dyrby, Orientationally invariant indices of axon diameter and density from diffusion MRI, Neuroimage 52 (2010) 1374–1389.

[32] E. Panagiotaki, T. Schneider, B. Siow, M.G. Hall, M.F. Lythgoe, D.C. Alexander, Compartment models of the diffusion MR signal in brain white matter: a taxonomy and comparison, Neuroimage 59 (2012) 2241–2256.

[33] J.-D. Tournier, C.-H. Yeh, F. Calamante, K.-H. Cho, A. Connelly, C.-P. Lin, Resolving crossing fibres using constrained spherical deconvolution: validation using diffusion-weighted imaging phantom data, Neuroimage 42 (2008) 617–625.

[34] J.S.W. Campbell, K. Siddiqi, V.V. Rymar, A.F. Sadikot, G.B. Pike, Flow-based fiber tracking with diffusion tensor and q-ball data: validation and comparison to principal diffusion direction techniques, Neuroimage 27 (2005) 725–736.

[35] C. Poupon, B. Rieul, I. Kezele, M. Perrin, F. Poupon, J.-F. Mangin, New diffusion phantoms dedicated to the study and validation of high-angular-resolution diffusion imaging (HARDI) models, Magnet. Reson. Med. 60 (2008) 1276–1283.

[36] L.M. Burcaw, E. Fieremans, D.S. Novikov, Mesoscopic structure of neuronal tracts from time-dependent diffusion, Neuroimage 114 (2015) 18–37.

[37] H.-H. Lee, G. Lemberskiy, E. Fieremans, D.S. Novikov, Estimation of fiber packing correlation length by varying diffusion gradient pulse duration, Proc. Int. Soc. Magnet. Reson. Med. 24 (2016) 2021.

[38] Y. Assaf, T. Blumenfeld-Katzir, Y. Yovel, P.J. Basser, AxCaliber: a method for measuring axon diameter distribution from diffusion MRI, Magnet. Reson. Med. 59 (2008) 1347–1354.

[39] E. Fieremans, J.H. Jensen, J.A. Helpern, White matter characterization with diffusional kurtosis imaging, Neuroimage 58 (2011) 177–188.

[40] H. Zhang, T. Schneider, C.A. Wheeler-Kingshott, A.D. C, NODDI: practical in vivo neurite orientation dispersion and density imaging of the human brain, Neuroimage 61 (2012) 1000–1016.

[41] D. Benjamini, M.E. Komlosh, L.A. Holtzclaw, U. Nevo, P.J. Basser, White matter microstructure from nonparametric axon diameter distribution mapping, Neuroimage 135 (2016) 333–344.

[42] E.A.H. von dem Hagem, R.M. Henkelman, Orientational diffusion reflects fiber structure within a voxel, Magnet. Reson. Med. 48 (2002) 454–459.

[43] C.-P. Lin, V.J. Wedeen, J.-H. Chen, C. Yao, W.-Y.I. Tseng, Validation of diffusion spectrum magnetic resonance imaging with manganese-enhanced rat optic tracts and ex vivo phantoms, Neuroimage 19 (2003) 482–495.

[44] N. Yanasak, J. Allison, Use of capillaries in the construction of an MRI phantom for the assessment of diffusion tensor imaging: demonstration of performance, Magnet. Reson. Imag. 24 (2006) 1349–1361.

[45] D. Morozov, L. Bar, N. Sochen, Y. Cohen, Modeling of the diffusion MR signal in calibrated model systems and nerves, NMR Biomed. 26 (2013) 1787–1795.

[46] D.S. Novikov, S.N. Jespersen, V.G. Kiselev, E. Fieremans, Quantifying brain microstructure with diffusion MRI: theory and parameter estimation, 2016, arXiv:1612.02059.

[47] Molex™ Microcapillaries <http://www.molex.com/molex/products/group>.

[48] E.O. Stejskal, J.E. Tanner, Spin diffusion measurements: spin echoes in the presence of a time-dependent field gradient, J. Chem. Phys. 42 (1965) 288–292.

[49] S. Vellmer, R. Stirnberg, D. Edelhoff, D. Suter, T. Stoecker, I.I. Maximov, Comparative analysis of isotropic diffusion weighted imaging sequences, J. Magnet. Reson. 275 (2017) 137–147, http://dx.doi.org/10.1016/j.jmr.2016.12.011.

[50] S. Vellmer, D. Edelhoff, D. Suter, I.I. Maximov, Fast mean diffusion imaging (FAMEDI) using microcapillary-based phantoms, Magnet. Reson. Mater. Phys., Biol. Med. 29 (2016) 547–548.

[51] S. Eriksson, S. Lasic, D. Topgaard, Isotropic diffusion weighting in PGSE NMR by magic-angle spinning of the q-vector, J. Magnet. Reson. 226 (2013) 13–18.

[52] C.F. Westin, H. Knutsson, O. Pasternak, F. Szczepankiewicz, E. Özarslan, D. van Westen, C. Mattisson, M. Bogren, M.J. O'Donnell, M. Kubicki, D. Topgaard, M. Nilsson, Q-space trajectory imaging for multidimensional diffusion MRI of the human brain, Neuroimage 135 (2016) 345–362.

[53] M.G. Hall, D. Alexander, Convergence and parameter choice for Monte-Carlo simulations of diffusion MRI, IEEE Trans. Med. Imag. 28 (2009) 1354–1364.

[54] M. Holz, S.R. Heil, A. Sacco, Temperature-dependent self-diffusion coefficients of water and six selected molecular liquids for calibration in accurate 1H NMR PFG measurements, Phys. Chem. Chem. Phys. 2 (2000) 4740–4742.

[55] D.J. Ozer, Correlation and the coefficient of determination, Psychol. Bull. 97 (1985) 307.

[56] P.P. Mitra, P.N. Sen, L.M. Schwartz, P. Le Doussal, Diffusion propagator as a probe of the structure of porous media, Phys. Rev. Lett. 68 (1992) 3555–3558.

[57] M.E. Komlosh, E. Özarslan, M.J. Lizak, F. Horkay, V. Schram, N. Shemesh, Y. Cohen, P.J. Basser, Pore diameter mapping using double pulsed-field gradient MRI and its validation using a novel glass capillary array phantom, J. Magnet. Reson. 208 (2011) 128–135.

[58] L. Avram, E. Özarslan, Y. Assaf, A. Bar-Shir, Y. Cohen, P.J. Basser, Three-dimensional water diffusion in impermeable cylindrical tubes: theory versus experiments, NMR Biomed. 21 (2008) 888–898.

[59] B. Siow, I. Drobnjak, A. Chatterjee, M.F. Lythgoe, D.C. Alexander, Estimation of pore size in a microstructure phantom using the optimised gradient waveform diffusion weighted NMR sequence, J. Magnet. Reson. 214 (2012) 51–60.

[60] P.P. Mitra, P.N. Sen, Effects of microgeometry and surface relaxation on NMR pulsed-field-gradient experiments: Simple pore geometries, Phys. Rev. B 45 (1992) 143–156.

[61] M. Nilsson, J. Lätt, E. Nordh, R. Wirestam, F. Ståhlberg, S. Brocksted, On the effects of a varied diffusion time in vivo: is the diffusion in white matter restricted?, Magnet Reson. Imag. 27 (2009) 176–187.

[62] S. Lanzafame, M. Giannelli, F. Garaci, R. Floris, A. Duggento, M. Guerrisi, N. Toschi, Differences in Gaussian diffusion tensor imaging and non-Gaussian diffusion kurtosis imaging model-based estimates of diffusion tensor invariants in the human brain, Med. Phys. 43 (2016) 2464.

[63] T. Niendorf, R.M. Dijkhuizen, D.G. Norris, M. van Lookeren Campagne, K. Nicolay, Biexponential diffusion attenuation in various states of brain tissue: implications for diffusion-weighted imaging, Magnet. Reson. Med. 36 (1996) 847–857.

[64] M.R. Lee, I.Y. Phang, Y. Cui, Y.H. Lee, X.Y. Ling, Shape-shifting 3d protein microstructures with programmable directionality via quantitative nanoscale stiffness modulation, Small 6 (2015) 740–748.

[65] C. Guise, M.M. Fernandes, J.M. Nobrega, S. Pathak, W. Schneider, R. Fangueiro, Hollow polypropylene yarns as a biomimetic brain phantom for the validation of high-definition fiber tractography imaging, Appl. Mater. Interfaces 8 (2016) 29960–29967.

[66] M.S. Vinding, C. Laustsen, I.I. Maximov, L.V. Søgaard, J.H. Ardenkjær-Larsen, N. C. Nielsen, Dynamic nuclear polarization and optimal control spatial-selective ^{13}C MRI and MRS, J. Magn. Reson. 227 (2013) 57–61.

[67] L.V. Søgaard, F. Schilling, M.A. Janich, M.I. Menzel, J.H. Ardenkjær-Larsen, In vivo measurement of apparent diffusion coefficients of hyperpolarized 13C-labeled metabolites, NMR Biomed. 27 (2014) 561–569.

[68] I. Drobnjak, D.C. Alexander, Optimising time-varying gradient orientation for microstructure sensitivity in diffusion-weighted MR, J. Magnet. Reson. 212 (2011) 344–354.

[69] G. Lemberskiy, E. Fieremans, S.H. Baete, M.A. Cloos, D.S. Novikov, Validation of surface-to-volume ratio measurements derived from oscillating gradient spin echo on a clinical scanner using anisotropic fiber phantoms NMR in Biomedicine, 2017, e3708. https://doi.org/10.1002/nbm.3708.

[70] E.D. André, F. Grinberg, E. Farrher, I.I. Maximov, N.J. Shah, C. Meyer, M. Jaspar, V. Muto, C. Phillips, E. Balteau, Influence of noise correction on intra- and inter-subject variability of quantitative metrics in diffusion kurtosis imaging, PLoS One 9 (4) (2014) e94531, http://dx.doi.org/10.1371/journal.pone.0094531.